Key Engineering Materials
ISSN: 1662-9795, Vol. 926, pp 159-167

Submitted: 2021-12-08
Revised: 2022-01-25
Accepted: 2022-02-18
Online: 2022-07-22

Maximizing the Resolution Range of Additive-Manufactured Miniature-Scale Force-Sensing Devices for Biomedical Applications

Luca Quagliato[1,a], Soo Yeon Kim[1,b] and Seok Chang Ryu[1,c,*]

[1]Division of Mechanical and Biomedical Engineering, Ewha Womans University,
52 Ewhayeodae-gil, Daehyeon-dong, Seodaemun-gu, 03760 Seoul, South Korea

[a]lucaq@ewha.ac.kr, [b]nanisy08@ewhain.net, [c]scryu@ewha.ac.kr

Keywords: Customized force sensor; sensor geometry optimization; additive manufacturing; curing conditions; biomedical application.

Abstract. This research presents a methodology for the design and manufacturing of miniature-scale force-sensing devices based on an additive manufactured sensor structure, coupled with strain gauge measuring elements, hereafter referred to as measuring device (MD). The proposed MD has been designed and manufactured to maximize the resolution of the steering force measurement in active needles utilized in biomedical applications. The force resolution is defined as the variation of the signal output of the four strain gauges bridge for predetermined increases of the applied force. By means of the proposed approach, the geometry and curing conditions of the sensor structure that allows achieving the maximum allowed deformation for the strain gauges, in the regions where they are installed on the sensor structure, can be defined a-priori, allowing to maximize the resolution of the measured force signal. The proposed methodology has been developed considering a sensor thickness ranging from 1 to 5mm and curing conditions varying from no curing up to 80°C for 120 minutes and showed that, by utilizing the proposed methodology, the measurable force range can be adjusted in the 0.1N~12.8N range with a relevant maximum and minimum resolutions ranging from 712.2 unit/N (force range : 0.1N~5N) to 362.2 unit/N (force range : 0.1N~12.8N), respectively.

1. Introduction

The interest of both academia and industry towards the additive manufacturing (AM) process has seen an exponential growth in the last years thanks to the possibility of achieving high customization without the need for costly manufacturing tools [1-4]. Although AM is a highly versatile process, it also comes with a complex interaction between component geometry, manufacturing, and curing conditions [5, 6]. Concerning this issue, Kok et al. [7] presented a critical review of the anisotropy and heterogeneity of the microstructure developing in powder, wire, and sheet-based additive manufacturing process and showed how the process parameters employed have a strong influence on the microstructure distribution developing in the component, thus on the overall mechanical performances.

This material-process-performances interaction is even more articulated and intertwined for the case of the additive manufacturing process of polymeric materials, where the post-process curing operation has a strong influence on the resulting performances and is inevitably coupled with the component geometry [8, 9]. This aspect has been addressed in Chantarapanich et al. [10] where the effect of the component geometry, the deposition strategy, in terms of the orientation between the growing direction with respect to the main load application direction, and of the curing conditions on the mechanical properties of tensile specimens have been investigated. However, one of the main limitations of this study is represented by the neglect of the curing penetration depth, a fact that influences the uniformity of the mechanical properties within the component.

In particular, the ultraviolet (UV) exposition curing process, normally utilized to achieve photopolymerization in SLA (stereolithography apparatus), has shown to be constrained by the penetration depth of the UV rays into thick elements [11], a fact that promotes a non-uniform distribution of the mechanical properties of the material throughout its thickness [12]. In-depth curing of thick structures can be achieved by consecutive curing phases [13] but this might have an effect on the already fully cured polymeric material by altering its mechanical properties, with consequent

embrittlement of the outer layers of the structure. On the other hand, if the geometry of the component is considered along with the curing conditions, a reasonable estimation of the overall and local mechanical properties, as well as of its performances, can be carried out. Henceforth, as carried out in the research presented in this paper, if an accurate design and manufacturing of AM components are aimed to be achieved, both the effect of the geometry, in terms of its thickness distribution, and the curing conditions, in terms of curing temperature and time, must be accounted for as driving force parameters for the evaluation of the mechanical performances of the manufactured component.

Aside from its well-known potentials, advanced manufacturing techniques, such as the AM process, are naturally interconnected to highly researched topics of today's academic world, such as flexible sensors and soft robotics, where customization is one of the most important keywords [14, 15]. As previously mentioned, the versatility of the AM process makes it a perfect manufacturing technique to produce highly customized sensors employed in various fields. To this aim, Rahman et al. [16] utilized an Aerosol Jet-based AM technique to realize capacitive touch sensors with high bending capability to utilize in human-machine interactions. In addition to that, Bird and Ravindra [17] showed how AM-based sensors represent the future of status monitoring of military personnel since they can be optimized to a specific application and according to the physiology of the user. AM-based sensors represent an innovative and yet complex field of research but, at the same time, offer several advantages that, if well exploited, can lead to high-performance applications.

Henceforth, in the research presented in this paper, an AM sensor structure connected to a four mm-scale strain gauges has been developed to measure the force required to steer active needle utilized in biomedical applications, Fig. 1a.

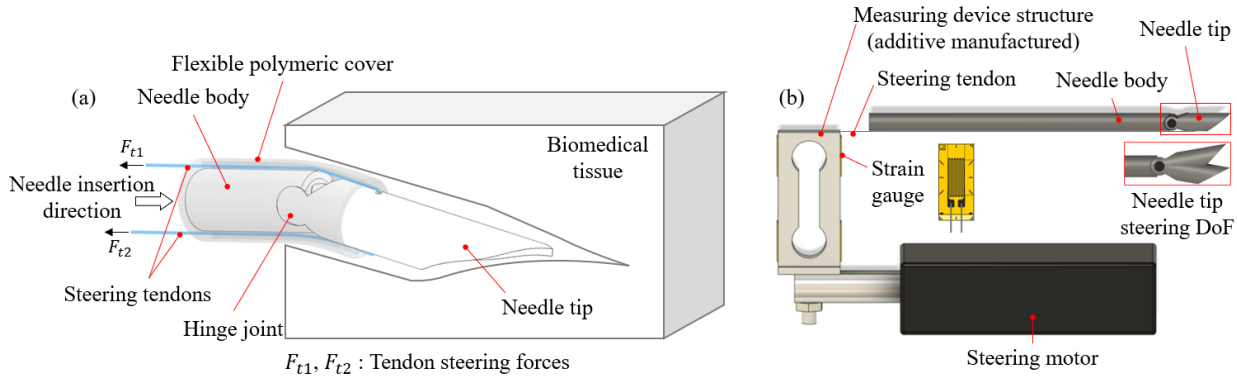

Figure 1 – (a) Schematic representation of an active needle insertion into a biomedical tissue and (b) designed measuring device with the connection with the tendon steering motor.

Active needles offer several advantages in comparison to standard (passive) ones since they allow for a controlled trajectory adjustment during the insertion into the tissue based on the inputs provided by the medical personnel operating the device [18, 19]. On the other hand, the measurement of the steering force required to achieve a specific location in the tissue can also be linked to the mechanical properties of the tissue material, with potential diagnostic applications. Nevertheless, due to the relatively low elastic modulus of biomedical tissues (skin, muscle, fat, etc.), which might also vary from patient to patient, an accurate measurement of possible variation of the tissue composition is intrinsically linked to the resolution of the employed sensor.

To this aim, in this paper, the tendon force measuring device (Fig. 1b) has been designed and manufactured considering different maximum measurable forces to maximize the strain gauge signal output variation caused by a change in the tendon force. To achieve this goal, the effect of thickness, curing temperature, and curing time on the tensile and compressive mechanical properties of additively manufactured MD-R001CR material (Acrylate polymer) has been investigated considering tensile and compression specimens having a cross-section ranging from 1mm to 5mm and curing conditions ranging from no curing to 80°C for 120 minutes. The results shall show how, by simultaneously controlling both geometry and the curing conditions, a value close to the maximum allowed strain for the employed GFLAB-3-50-5LJC-F strain gauges can be achieved when the maximum target force is applied. The defined procedure has been applied considering various

maximum allowable forces and verified by both FEM simulations and laboratory experiments on measuring device structures manufactured by employing different curing conditions. From the results of the investigations it has been confirmed that by considering the influence of both geometry and curing conditions on the mechanical performances of additive manufactured measuring device sensor structure, the maximum measurable steering force range can be adjusted from a 0.1N to a 12.8N with a relevant resolution range from 712.2 unit/N to 362.2 unit/N.

2. Geometry and Curing Conditions-Dependent Material Properties

The material employed for the manufacturing of the measuring device structure introduced in Fig. 1b, the focus of the research presented in this paper, is realized with the Acrylate polymer MD-R001CR material, manufactured by ApplyLabWork, and dedicated to SLA machines. To investigate the influence of geometry, in terms of thickness, and of the curing conditions, in terms of curing temperature and exposition time, on the elastic properties of the considered MD-R001CR material, five tensile and five compression specimens have been designed and manufactured, Fig. 2. All the specimens have a circular cross-section to promote uniform in-depth curing along their cross-sections. The curing of the specimens, as well as of the measuring device structure, presented in the following section of the paper, have been carried out by a uniform UV light exposition and by employing the FormCure machine with a power light source of 385~405nm.

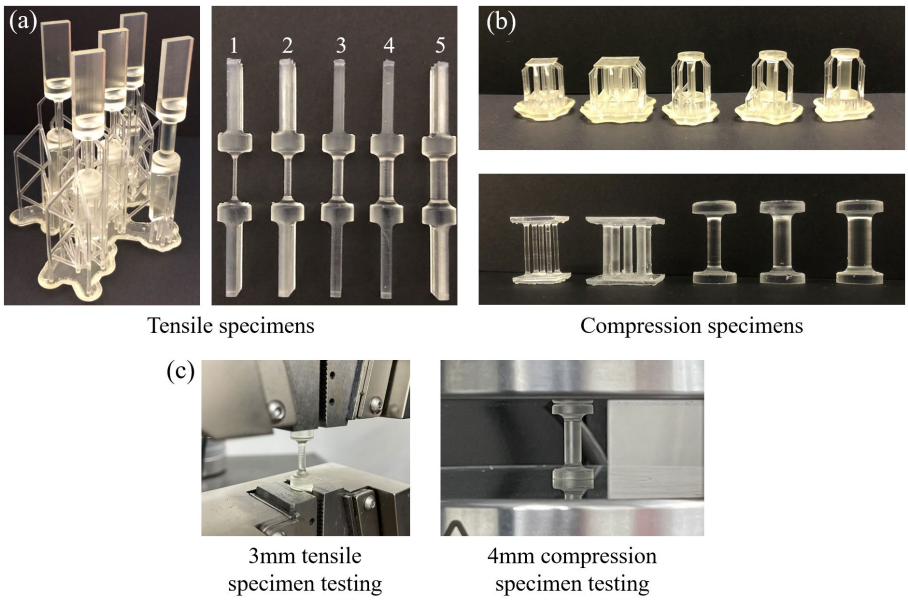

Figure 2 – (a) Tensile and (b) compression specimens manufactured by AD process. (c) Tensile and compression specimens during the relevant material properties characterization tests.

Both tensile and compression specimens have been tested employing the Instron 5969 Dual Column Testing System, Fig. 2c, under quasi-static conditions at a speed (both tensile and compressive) equal to 1 mm/min until failure, for the case of the tensile specimens, and until extensive buckling appeared, for the case of the compression specimens. To avoid stress concentration in the jig regions of the tensile specimens, a large radius has been added during the design process whereas, for the case of the compressive specimens, to avoid severe buckling during the elastic deformation phase, a multiple specimen configuration has been considered for the 1mm and 2mm cases, Fig. 2b.

The tensile-compressive experimental engineering stress-strain curves, for the no-curing and 80°C for 120 minutes curing conditions, for the five considered specimens geometries, are reported in Fig. 3a and 3b, respectively. For the case of the previously mentioned multiple specimen configuration (compressive specimens of 1mm and 2mm diameters), the engineering stress has been calculated considering the overall specimens area.

In order to better understand the effect of both geometry and curing conditions on the elastic properties (Young's modulus) of the considered material, tensile and compressive responses

measured from the whole tested specimens are summarized in Fig. 4a and 4b. The curing energy reported in Fig. 4 has been calculated considering the overall energy provided by the system to the specimen during the curing by means of radiation heat transfer. Globally, the considered curing conditions and geometry range allows for a variation of the tensile Young's modulus from 0.71 GPa up to 1.45 GPa, and from 0.55 GPa to 1.96 GPa for the compressive elastic behavior.

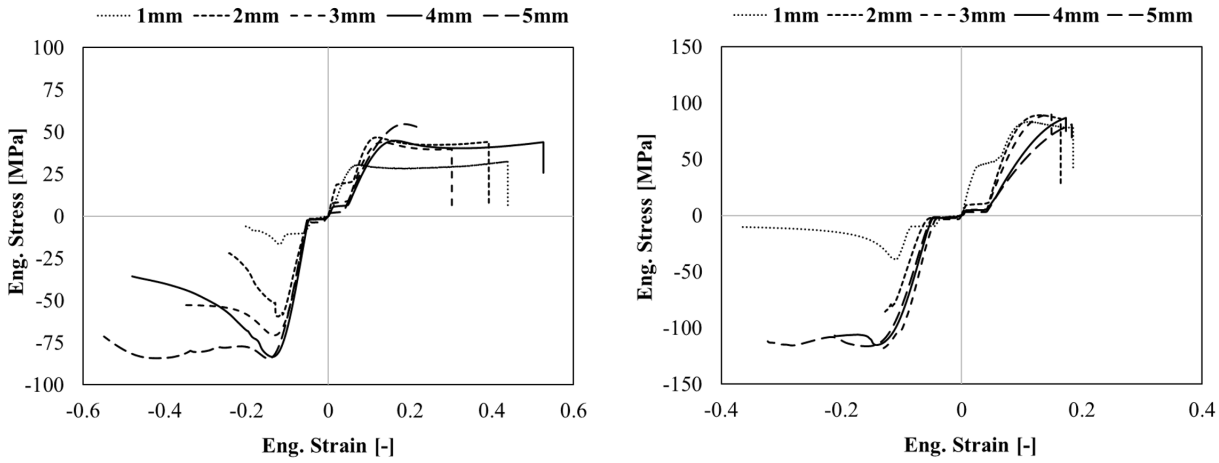

(a) Tensile-compressive behavior of no-cured specimens

(b) Tensile-compressive behavior of specimens cured at 80° C for 120 minutes

Figure 3 – Tensile and compressive engineering stress-strain curves for (a) no curing (as manufactured) specimens and (b) 80°C for 120min curing condition specimens.

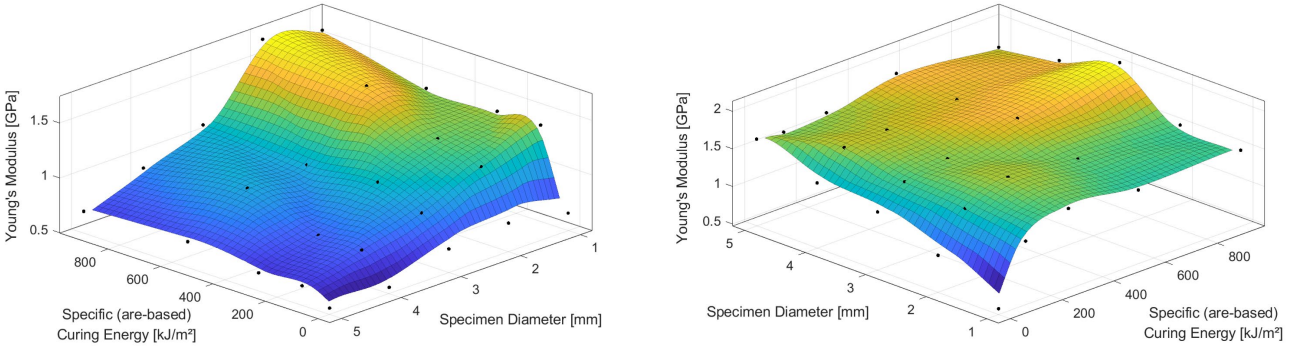

(a) Tensile specimens

(b) Compression specimens

Figure 4 – Influence of geometry and curing conditions (in terms of curing energy) on the elastic modulus of (a) tensile and (b) compression specimens.

3. Experimental and Finite Element Investigation Procedures

Considering the results of the experimental investigations reported in the previous section of the paper, the measuring device structure, previously introduced in Fig. 1b, has been designed with an initial thickness of strain gauges installation regions equal to 1.5 mm, as shown in Fig. 5a, where also the remaining dimensions of the structure are reported. The sensitive regions of the measuring device structure, represented by the locations where the strain gauges are installed and the nearby regions, have been all modeled with a thickness between 1.5 mm and 2.2 mm to promote a uniform material properties distribution, while also granting sufficient strength. On the contrary, to achieve high stiffness and strength, the connecting plate and screw, at the bottom of the measuring device structure, have been designed with a thickness ranging from 3 to 5mm.

The working principle of the designed measuring system, including the measuring device and the signal processing and post-processing unit, is summarized in Fig. 5b. The four strain gauges (GFLAB-3-50-5LJC-F, Tokyo Measuring Instruments Lab) are connected in a Wheatstone bridge configuration supplied with a stabilized 3.3V power source whereas the output signals are acquired

by an ARDUINO UNO controller with a data sampling frequency of 20 Hz. The wire extending from the measuring device top surface to the weight support element is realized with an Aramid Sewing Thread 1200D having a Young's modulus of E = 112.4GPa, thus it can be regarded as a rigid element that does not affect the overall stiffness of the system. The testing configuration reported in Fig. 5b is the one utilized for the calibration of the measuring device system, required to link the electric signal recorded by the ARDUINO interface with the relevant force measurement.

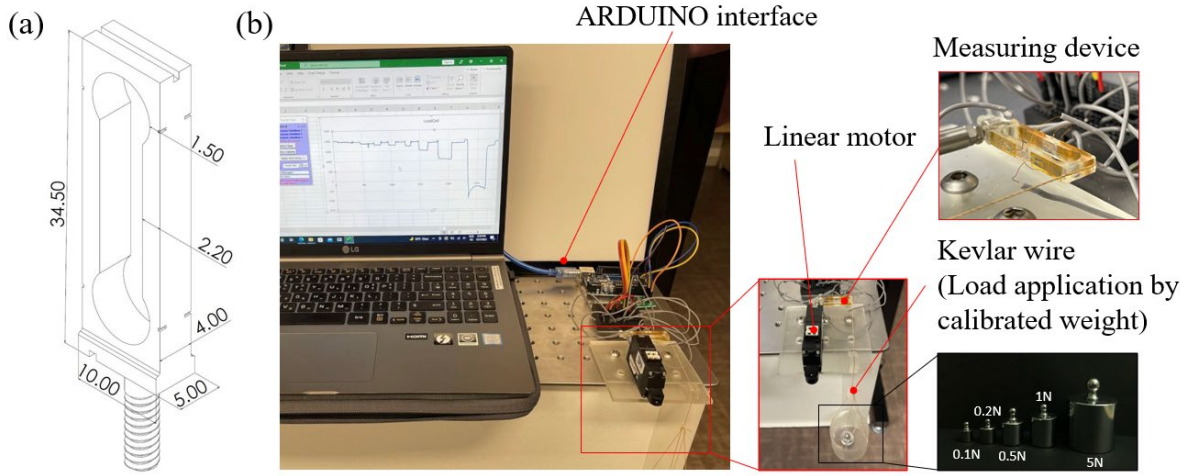

Figure 5 – (a) Dimensions of the measuring device structure with relevant thickness distribution ranges and (b) experimental set-up utilized for the calibration of the voltage-force relationship.

During the calibration tests, the force applied to the measuring device has been progressively increased from 0.1 N to 5 N in order to verify the variation of the output signal of the strain gauges bridge, considered for the estimation of the resolution of the measuring device.

Considering the dimensions of the measuring device structure (Fig. 5a), the curing conditions-dependent Young's moduli derived from the mechanical testing (Fig. 4), and the strain gauge transverse sensitivity provided by the manufacturer, equal to 2.10±2%, the voltage output of the Wheatstone bridge can be linked to the relevant force measurement by means of Eq. (1). In this research, four different curing conditions have been applied to the measuring device geometry reported in Fig. 5a and are listed in Table 1.

$$F = \frac{\left(2bt^2\right)\cdot E\cdot \Delta V}{\left(3L\right)\cdot \alpha \cdot V_{in}} \tag{1}$$

Table 1 – Curing conditions applied to the measuring device structure.

Case numbering	Curing temperature	Curing time
E1	No curing	No curing
E2	40°C	60 min
E3	60°C	120 min
E4	80°C	120 min

The results relevant for the calibration of four measuring devices, manufactured considering the curing conditions of Table 1, along with the relevant resolutions, in terms of digital signal variation for the predefined increase of the applied force, are reported in the following section of the paper.

Nevertheless, since no literature contributions seem to analyze the steering force ranges for active needles application during the insertion into soft tissues, a preliminary FEM investigation of the strain distributions arising on the strain gauge regions have been carried out in ABAQUS/Standard considering the different tensile and compressive behaviors reported in Fig. 4.

Since the interest is focused on the elastic material behavior, only the experimentally determined Young's moduli and a Poisson's ratio equal to 0.37 have been inputted in the FEM model. The assembly between the measuring device and the linear motor utilized for the steering of the needle

tip tendons and the FEM model implementation, with relevant simplifications, are reported in Fig. 6a and 6b respectively. The model has been meshed with quadratic order tetrahedral elements having a global length equal to 0.3 mm for a total of 246,653 elements.

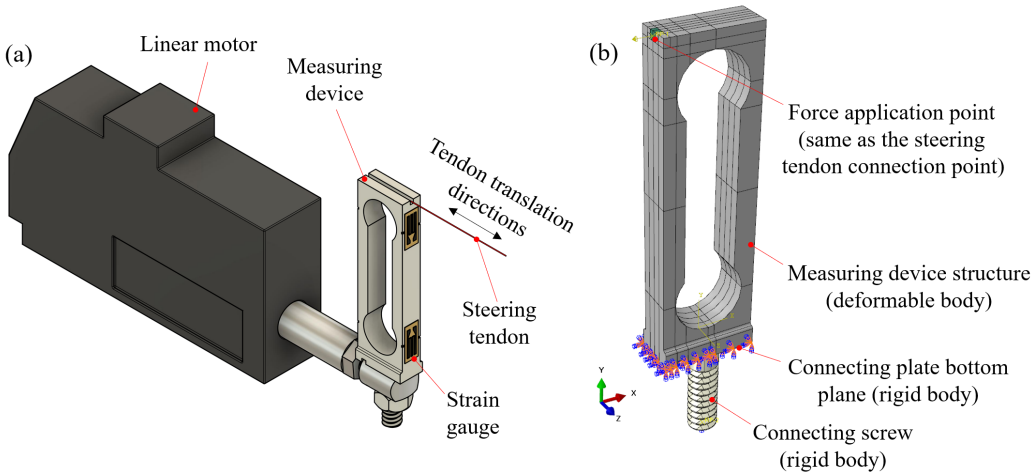

Figure 6 – (a) Assembly conditions between the measuring device structure and the linear motor utilized to apply steering to the tendons and (b) implemented FEM model details.

4. Results and Discussion

In this section, the results of the preliminary FEM analysis are firstly reported to provide an insight into the strain distribution arising in the regions of the measuring device structure where the strain gauges are installed. Since the employed strain gauges have a strain limit equal to 0.03, this preliminary analysis is required to have a first indication of whether the applied force, coupled with the tensile-compressive material behavior of the considered curing condition, makes the strain gauges to reach and pass their operational limit. The second part of the results section summarizes the results of the experimental calibrations on the measuring device structures where the four curing conditions reported in previous Table 1 have been applied, along with the relevant resolution values.

As concerns the FEM analysis, four different curing conditions reported in Table 1 have been considered along with the relevant tensile and compressive Young's moduli, according to Fig. 4. The summary of the results relevant for the variation of the equivalent elastic von Mises strain, averaged in the region where the strain gauges are installed, is reported in Fig. 7 along with a representative image of the LE (linear elastic) strain distribution on the E=1.28 GPa (40°C, 60min curing) and 7N load conditions.

Considering the 0.03 strain limit of the employed strain gauges, a variation of the tensile and compressive elastic behaviors of the measuring device structure, as a consequence of different curing conditions, result in different maximum measurable forces. For instance, the E1 condition allows for a maximum measurable force equal to approximately 5N and can therefore be employed for the case of relatively small steering forces in relatively soft tissue. On the other hand, if higher loads are aimed to be measured, a curing condition must be applied and, according to the energy provided to the measuring device structure, the maximum measurable force varies from 9N (E2) to 12.8N (E4).

In addition to that, if higher forces are aimed to be measured, the thickness of the measuring device, considered constant in this analysis, can be increased to promote a lower deformation in the regions of the measuring device structure where the strain gauges are installed.

By considering the results presented in Fig. 7b, the calibration experiments have been carried out considering a minimum load of 0.1N and a maximum load equal to 5N. By considering this approach, the force range is defined according to the maximum force for the no curing conditions and allows for a more accurate estimation of the force measurement resolution.

The calibration procedure has been carried out employing the apparatus shown in Fig. 5b and by the progressive addition of higher loads on the weight support, from the initial values of 0.1N up to 5N. An example of the digital signal output, for the case of a measuring device structure cured at

80°C for 120min, is reported in Fig. 8a. For the sake of clarity, the results reported in Fig. 8a are relevant for loads ranging from 0.1N to 1N. Besides, the time from the initial load application (signal increase) to the load removal (signal drop) has been considered to allow the system to restore its equilibrium. The results relevant for the calibration experiment of the four curing conditions reported in Table 1 are summarized in Fig. 8b, where the force measurement resolutions, calculated as the slope of the four interpolation curves, are also reported.

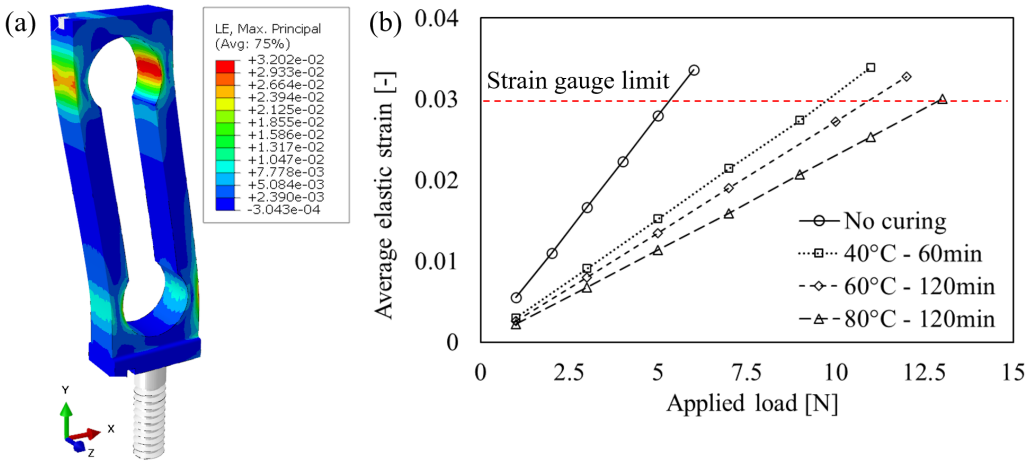

Figure 7 – (a) Equivalent von Mises strain distribution (LE) on the measuring device structure e when considering the tensile and compressive elastic behavior at 40°C, 60min curing, and (b) variation of the LE strain for increasing loads and different curing conditions (Table 1).

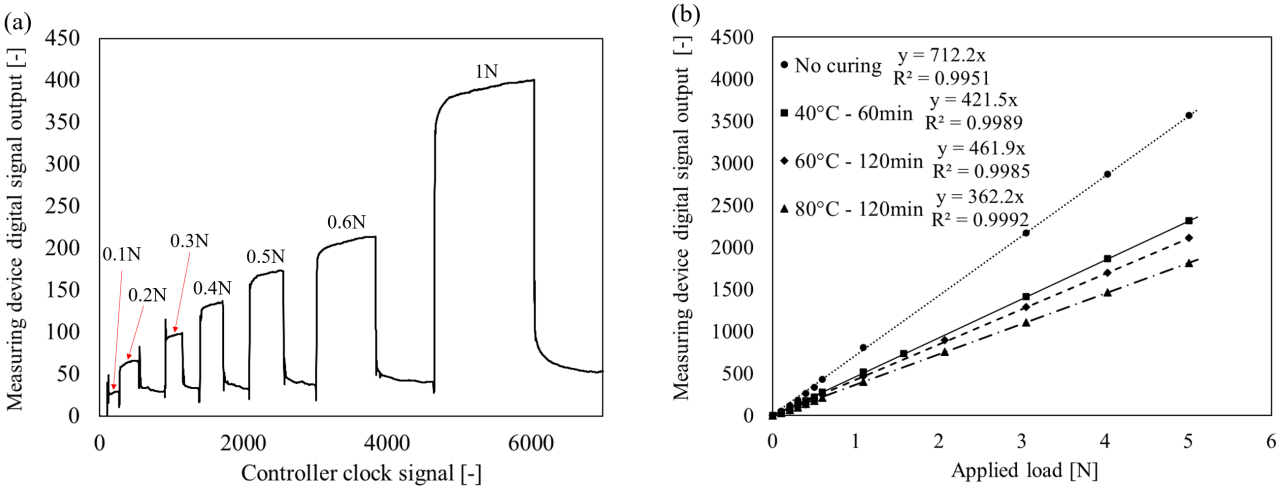

Figure 8 – (a) Increase of the digital signal output from the converted analogic signal of the measuring device strain gauge bridge for increasing applied loads (80°C, 120min curing) and (b) summary of the digital signal variation for the four tested conditions from 0.1N to 5N.

As also previously highlighted in the FEM investigation results, if no curing is applied to be measuring design structure, the highest variation of the signal output from the strain gauges bridge can be achieved, at the expense of the maximum measurable force. For this case, a force increase of 1N creates a signal variation equal to 712.2 (slope of the regression curve), a fact which makes this configuration to be highly sensitive even to very small force variations, of vibrations, on the steering tendons. On the other, the application of increasing curing energies, by both longer time or higher temperature, allows stiffening of the measuring device structure, with the consequent lower signal variation for the same increase in force. It is also interesting to notice the huge variation in the force measurement resolution from the no curing to the 40°C - 60min curing conditions, a fact which suggests the need for further investigation in the region between these two values.

By considering altogether the results presented in Fig. 7b and 8b two important aspects ought to be underlined. First, considering a preliminary FEM analysis is important to avoid possible overload

for both strain gauges and the MD structure. For this reason, the determination of the tensile and compressive mechanical properties of the considered material, under different conditions, is essential for the accurate design of the sensor structure. As also highlighted in the introduction section, in polymer-based additive manufacturing, geometry and manufacturing conditions are not separated entities but, instead, should be both accounted for simultaneously during the design stage.

Secondly, although a reasonable accurate design of additive manufactured sensor structures can be carried out by employing the procedure detailed in this research, more work should be carried out towards the direction of considering a visco-elastic material model instead of a fully elastic. The presence of a visco-elastic material behavior is clear from the results reported in Fig. 8a, where, after the initial load application, a slight increase in the measured signal has been observed.

Summary

The research presented in this paper detailed a methodology for the design of small-scale sensor structures for biomedical applications, manufactured through the additive manufacturing process. From the results of both FEM and experimental investigations, it was possible to define a correlation between the curing conditions applied to the sensor structure and the resolution in the force measurement, estimated in the 712.2 unit/N~362.2 unit/N range, as well as of the maximum measurable force (0.1N~12.8N). The results summarized in this paper are relevant for a larger research project whose aim is the correlation between the steering force required by an active needle to reach a specific spatial position during medical examinations and the mechanical properties of the tissue being penetrated. To this aim, in order to achieve comparable force measurement resolutions for different typologies of tissues (i.e. skin, muscle, fat, etc.), different curing conditions and various sensor geometries are aimed to be designed and manufactured using the procedure presented in this paper.

Acknowledgements

This research was supported by Basic Science Research Program through the National Research Foundation of Korea(NRF) funded by the Ministry of Education(2019R1I1A1A01062323). Prof. Dr. Luca Quagliato was supported by RP-Grant 2021 of Ewha Womans University. Finally, the authors would also like to thank Ms. Yoonsue Choi for the help provided in developing the ARDUINO control interface.

References

[1] D. Lehmhus, C. Aumund-Kopp, F. Petzoldt, D. Godlinski, A. Haberkorn, V. Zöllmer, M. Busse, Customized Smartness: A Survey on Links between Additive Manufacturing and Sensor Integration, Procedia Technol. 26 (2016) 284–301..

[2] L. Chen, Y. He, Y. Yang, S. Niu, H. Ren, The research status and development trend of additive manufacturing technology, Int. J. Adv. Manuf. Technol. 89 (2017) 3651–3660.

[3] O. Abdulhameed, A. Al-Ahmari, W. Ameen, S.H. Mian, Additive manufacturing: Challenges, trends, and applications, Adv. Mech. Eng. 11 (2019) 1–27.

[4] K. Rajaguru, T. Karthikeyan, V. Vijayan, Additive manufacturing-State of art, Mater. Today Proc. 21 (2020) 628–633.

[5] J. Bonada, A. Muguruza, X. Fernández-Francos, X. Ramis, Influence of exposure time on mechanical properties and photocuring conversion ratios for photosensitive materials used in Additive Manufacturing, Procedia Manuf. 13 (2017) 762–769.

[6] G. Liu, X. Zhang, X. Chen, Y. He, L. Cheng, M. Huo, J. Yin, F. Hao, S. Chen, P. Wang, S. Yi, L. Wan, Z. Mao, Z. Chen, X. Wang, Z. Cao, J. Lu, Additive manufacturing of structural materials, Mater. Sci. Eng. R Reports. 145 (2021) 100596.

[7] Y. Kok, X.P. Tan, P. Wang, M.L.S. Nai, N.H. Loh, E. Liu, S.B. Tor, Anisotropy and heterogeneity of microstructure and mechanical properties in metal additive manufacturing: A critical review, Mater. Des. 139 (2018) 565–586.

[8] S.C. Ligon, R. Liska, J. Stampfl, M. Gurr, R. Mülhaupt, Polymers for 3D Printing and Customized Additive Manufacturing, Chem. Rev. 117 (2017) 10212–10290.

[9] J. Zhao, Y. Yang, L. Li, A comprehensive evaluation for different post-curing methods used in stereolithography additive manufacturing, J. Manuf. Process. 56 (2020) 867–877.

[10] N. Chantarapanich, P. Puttawibul, K. Sitthiseripratip, S. Sucharitpwatskul, S. Chantaweroad, Study of the mechanical properties of photo-cured epoxy resin fabricated by stereolithography process, Songklanakarin J. Sci. Technol. 35 (2013) 91–98.

[11] C. Ebner, J. Mitterer, P. Eigruber, S. Stieger, G. Riess, W. Kern, Ultra-high through-cure of (meth)acrylate copolymers via photofrontal polymerization, Polymers 12 (2020) 1–12.

[12] C. Hofstetter, S. Orman, S. Baudis, J. Stampfl, Combining cure depth and cure degree, a new way to fully characterize novel photopolymers, Addit. Manuf. 24 (2018) 166–172.

[13] Y. Li, Q. Mao, X. Li, J. Yin, Y. Wang, J. Fu, Y. Huang, High-fidelity and high-efficiency additive manufacturing using tunable pre-curing digital light processing, Addit. Manuf. 30 (2019) 100889.

[14] A. Kumar, Methods and Materials for Smart Manufacturing: Additive Manufacturing, Internet of Things, Flexible Sensors and Soft Robotics, Manuf. Lett. 15 (2018) 122–125.

[15] X. Sui, J.R. Downing, M.C. Hersam, J. Chen, Additive manufacturing and applications of nanomaterial-based sensors, Mater. Today. 48 (2021) 135–154.

[16] M.T. Rahman, A. Rahimi, S. Gupta, R. Panat, Microscale additive manufacturing and modeling of interdigitated capacitive touch sensors, Sensors Actuators, A Phys. 248 (2016) 94–103.

[17] D.T. Bird, N.M. Ravindra, Additive manufacturing of sensors for military monitoring applications, Polymers 13 (2021) 1-12.

[18] S. Pattanshetti, S.C. Ryu, Design and fabrication of laser- machined hinge joints on miniature tubes for steerable medical devices, J. Mech. Robot. 10 (2018) 1–8.

[19] S. Pattanshetti, R. Sandstrom, A. Kottala, N.M. Amato, S.C. Ryu, Feasibility study of robotic needles with a rotational tip-joint and notch patterns, Proc. - IEEE Int. Conf. Robot. Autom. 2019-May (2019) 1534–1540.